Chapter 7
Quantum Mechanical Simulation of Electron Dynamics on Surfaces of Materials

Lei Cui, Rulin Wang, ChiYung Yam, GuanHua Chen, and Xiao Zheng

Abstract Understanding the electronic dynamics on surfaces of materials is fundamentally important for applications including nanoelectronics, inhomogeneous catalysis, and photovoltaics. Time-dependent density-functional theory (TDDFT) has been successfully applied to predict excited-state properties of isolated and periodic systems. However, it cannot address a system coupled to an environment or whose number of electrons is not conserved. To tackle these problems, TDDFT needs to be extended to accommodate open systems. This chapter provides a comprehensive account of TDDFT for open systems (TDDFT-OS), including both theoretical and practical aspects. The practicality and accuracy of TDDFT-OS method are demonstrated with two numerical examples: the time-dependent electron transport through a series of quasi-one-dimensional atomic chains and the real-time electronic dynamics on a two-dimensional graphene surface.

Keywords TDDFT · Open system · Real-time electronic dynamics · Electron transport · Surfaces of materials

7.1 Introduction

Electronic dynamics at the surfaces or interfaces of materials is fundamentally important for a wide range of applications, such as nanoelectronics, photovoltaics, and heterogeneous catalysis. For instance, how the photoexcited electrons transfer from the dye molecule to the semiconductor surface and then drain into the bulk [1] is

L. Cui · R. Wang · X. Zheng (✉)
Hefei National Laboratory for Physical Sciences at the Microscale & Synergetic Innovation Center for Quantum Information and Quantum Physics, University of Science and Technology of China, Hefei, Anhui 230026, China
e-mail: xz58@ustc.edu.cn

C. Yam
Beijing Computational Science Research Center, No. 3 He-Qing Road, Beijing 100084, China

G. Chen
Department of Chemistry, The University of Hong Kong, Pokfulam Road, Hong Kong, Hong Kong

S. Shankar et al. (eds.), *Computational Materials, Chemistry, and Biochemistry: From Bold Initiatives to the Last Mile*, Springer Series in Materials Science 284,
https://doi.org/10.1007/978-3-030-18778-1_7

essentially important for the efficiency of a dye-sensitized solar cell [2], and how a water-oxidation complex acquires electrons from a water molecule and feeds them into the supporting conductor is critical to its catalytic reactivity [3]. These systems can be considered as prototypical systems in which molecules are adsorbed on a surface of a material. The systems' functionality is crucially influenced by the real-time electronic processes on material surfaces. Therefore, quantum mechanical simulation at atomic level is very useful for understanding the key features of the real-time electronic dynamics and the underlying mechanisms.

Density functional theory (DFT) and its time-dependent extension, the time-dependent density functional theory (TDDFT), are very popular methods in many fields of modern sciences because of their excellent balance between computational cost and accuracy [4–7]. For any practical application of DFT or TDDFT, a realistic system's model always requires a boundary condition be explicitly or implicitly specified. Conventional DFT or TDDFT methods have been applied mostly to systems subject to two types of boundary conditions: the isolated boundary condition and the periodic boundary condition. The isolated boundary condition is suitable for atoms, molecules, clusters, etc. The periodic boundary condition covers nanotubes, polymers, crystals, etc. For isolated systems, the electron density falls off to zero at places infinitely away from the nuclei [8, 9], while for periodic systems, the electron density possesses the lattice translational invariance symmetry [10–15]. However, in many circumstances, the system of interest is neither isolated nor periodic. Consider, for example, a nanoelectronic device which is connected to macroscopic electrodes. A key property is its conductance, which is very challenging to characterize by conventional DFT or TDDFT methods. This is because it is impractical or inappropriate to treat the device-electrodes' composite system or just the device itself as either isolated or periodic, when there is electron current flowing through the device. For an accurate and efficient characterization of electron conduction, an ideal theoretical approach would allow one to focus on the current-carrying device of primary interest, while addressing the influence of macroscopic electrodes without drastically increasing the computational cost. In other words, the device can be regarded as a system which has an open boundary, while the electrodes constitute the "environment" coupled to the open system [16].

In both physics and chemistry, an open system is referred to as a system which is coupled to its surrounding environment; see Fig. 7.1 for a schematic diagram. The open system exchanges particles, energy, or phase with the environment through their interfaces. It is essentially important to characterize the static and dynamic properties of the open system by the complex influences of the environment. Because the environment is usually very (if not infinitely) large in realistic situations, an accurate and efficient theoretical treatment is rather challenging. Since it is always impractical to consider the entire composite system (open system plus environment), one can use appropriate quantum dynamical equations to describe the open system explicitly, while accounting for the dissipative environment in a statistical manner. In the framework of DFT and TDDFT, the Kohn–Sham reference system is of effective single-electron nature [17] and thus facilitates a formally exact statistical description of the environment.

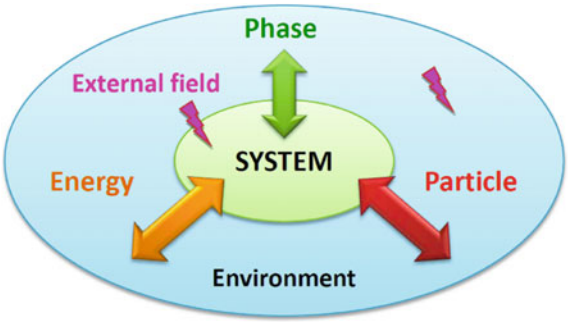

Fig. 7.1 Schematic illustration of an open quantum system coupled to the surrounding environment. The dissipative interactions between the system and environment. Reprinted with permission from [16]. Copyright 2013, Science China Press and Springer-Verlag Berlin Heidelberg

From the above examples, a method called the open-system TDDFT (TDDFT-OS) is built on a formally exact theoretical foundation [18–24] to extend the applicability of DFT and TDDFT to the realm of open systems. More importantly, the TDDFT-OS offers a unique advantage for the simulation of real-time electronic dynamics. Because electrons may enter or leave the system of primary concern, the total number of electrons inside the open boundary separating the system from its surrounding environment may change with time. Since both isolated and periodic models conserve the electron number, the variation in number of electrons is intrinsically forbidden for conventional TDDFT. In contrast, the TDDFT-OS can in principle characterize exactly the exchange of electrons between the open system and its environment.

The remainder of this chapter is organized as follows. We first validate the existence of a rigorous TDDFT-OS in Sect. 7.2.1. Then we try to establish a practical Kohn–Sham scheme in Sect. 7.2.2, with which numerical calculations can be carried out on realistic open systems. The dissipation functional, a vital quantity that addresses the complex system–environment dissipative interactions, is elaborated. We then introduce a variety of formalisms, which are designed to achieve an accurate and efficient evaluation of the dissipation functional. In Sect. 7.3, we demonstrate the practicality of a TDDFT-OS approach to simulate the electron transport through a quasi-one-dimensional (quasi-1D) atomic chain and the dynamics of an excess electron on a 2D graphene bilayer. Concluding remarks are finally given in Sect. 7.4.

7.2 Methodology

7.2.1 Existence of a Rigorous TDDFT for Open Systems

In 1981, Riess and Münch have assumed that the electron density distribution of the whole molecular system can be determined by any nonzero volume piece of ground-state electron density [25]. Such a conjecture has been extended by Mezey to a ground-state holographic electron density theorem (GS-HEDT) [26].

The GS-HEDT is proved by [22], and the mathematical machinery is called the real analyticity of ground-state electron density functions, which has been proved by Fournais et al. [27, 28] and Jecko [29] separately. A real analytic function is "extremely" smooth. It possesses derivatives of all orders, and its associated Taylor series converges consistently to the function values. The holographic property can be inferred by the function's real analyticity, which guarantees that the electron density inside any subsystem determines completely the electron density distribution in the entire $\vec{r}$-space.

A one-to-one mapping between the external potential $v(\vec{r})$ and ground-state electron density function inside any subsystem D, $\rho_D(\vec{r})$, can be established by the GS-HEDT. It validates the existence of a rigorous DFT for open systems. In principle, the electron density inside any subsystem D of nonzero volume is sufficient to determine any electronic property of the entire system.

The existence of TDDFT-OS has been explored by many researchers [18–24]. For instance, Burke, Car, and Gebauer have proved the existence of TDDFT for open systems by establishing a Runge–Gross-type theorem [30]. Yuen-Zhou et al. [23, 31] have extended the Runge–Gross theorem to open systems coupled to non-Markovian dissipative environment. Tempel et al. [24] have proved the existence of a TDDFT Kohn–Sham scheme for open systems. It should be emphasized that the open systems considered in these works have conserved numbers of electrons.

A more general theoretical framework named time-dependent holographic electron density theorem (TD-HEDT) has been proposed and proved by Chen et al. [18, 21, 22] which admits open systems that gain or lose electrons from or to the environment. Provided that the electron density at a certain t_0 and $\rho_D(\vec{r}, t_0)$, which is real analytic in $\vec{r}$-space, a one-to-one mapping between $\rho_D(\vec{r})$ and the external potential $v(\vec{r}, t)$ is established by the TD-HEDT after t_0. The TD-HEDT for time-dependent open systems parallels the Runge–Gross theorem for isolated systems, and it applies to the same phenomena and properties as those intended by the Runge–Gross theorem. Here, we address two important issues regarding the TD-HEDT. Firstly, for the TD-HEDT to be valid, the whole system which includes open system and its environment must be finite. The finiteness condition does not compromise the practicality of TDDFT-OS, because in practice, a finite system can be rather large in size. Therefore, TDDFT-OS is applicable to a microscopic open system coupled to macroscopic bulk material environment. Secondly, unlike the GS-HEDT, the proof of TD-HEDT does not involve any form of analytical continuation of electron density in $\vec{r}$-space, while the proof of GS-HEDT is based on continuation of the real analytic electron density function from within a region D to its outside. In any case, although in principle $\rho_D(\vec{r})$ determines uniquely and completely $\rho(\vec{r})$ of the entire system, the analytical continuation should not be taken as a practical scheme to extend electron density from an open system to its environment, as it is numerically extremely unstable, and unjustified for time-dependent systems for which the validity of real analyticity is unknown. The theoretical foundations of DFT and TDDFT for isolated and open systems are summarized in Fig. 7.2.

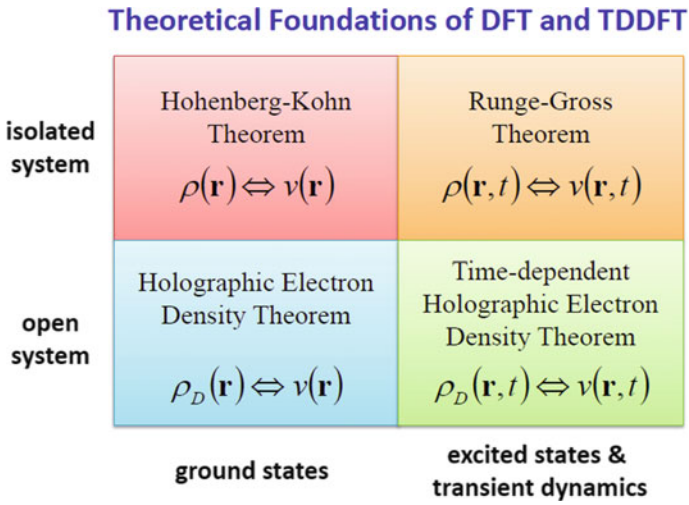

Fig. 7.2 .Schematic diagram summarizing the theoretical foundations of DFT (left column) and TDDFT (right column). The upper and lower rows apply to isolated and open systems, respectively. Reprinted with permission from [16]. Copyright 2013, Science China Press and Springer-Verlag Berlin Heidelberg

7.2.2 TDDFT Methods for Practical Calculations

(I) TDDFT formalisms for isolated, periodic, and open systems

For carrying out practical calculations on realistic systems, a formally exact and numerically efficient formulation of TDDFT is needed. For isolated systems, a TDDFT method has been developed with a time-domain formalism. A closed equation of motion (EOM), which uses the Kohn–Sham reduced single-electron density matrix of the total system $\boldsymbol{\sigma}$(t) as the basic variable [32, 33], has been derived,

$$i\dot{\boldsymbol{\sigma}}(t) = [\boldsymbol{h}(t), \boldsymbol{\sigma}(t)]. \tag{7.1}$$

Here, $\boldsymbol{h}(t)$ is the Kohn–Sham Hamiltonian matrix of the whole system, and the right-hand side square bracket denotes a commutator. In an atomic basis representation, the matrix elements of $\boldsymbol{\sigma}$ are defined as $\boldsymbol{\sigma}_{ij}(t) \equiv a_j^{\dagger}(t)a_i(t)$, where $a_j^{\dagger}(t)$ and $a_i(t)$ are the Heisenberg creation and annihilation operators for atomic orbitals $\chi_j(\vec{r})$ and $\chi_i(\vec{r})$, respectively. The time-dependent electron density is related to $\boldsymbol{\sigma}$ via $\rho(r,t) = \sum_{ij} \boldsymbol{\sigma}_{ij}(t)\left[\chi_i(\vec{r})\right]^* \chi_j(\vec{r})$. If both sides of (7.1) are Fourier transformed to the frequency domain while considering the linear response only, the conventional Casida's equation [34] is recovered.

A similar EOM works for periodic systems [35]:

$$i\dot{\boldsymbol{\sigma}}^{\vec{k}}(t) = \left[\boldsymbol{h}^{\vec{k}}(t), \boldsymbol{\sigma}^{\vec{k}}(t)\right]. \tag{7.2}$$

Here, $\vec{k}$ represents a point in the Brillouin zone. $\boldsymbol{\sigma}^{\vec{k}}(t) = \sum_{\vec{R}} e^{-i\vec{k}\vec{R}}\boldsymbol{\sigma}\left(t;\vec{R}\right)$, with $\vec{R}$ being the lattice vector which determines the translational symmetry of the periodic system. $\boldsymbol{\sigma}_{ij}\left(t;\vec{R}\right) \equiv a_j^{\dagger}\left(t;\vec{R}+\vec{R}'\right)a_i\left(t;\vec{R}'\right)$, where atomic orbitals $\chi_j\left(\vec{r}-\vec{R}-\vec{R}'\right)$ and $\chi_i\left(\vec{r}-\vec{R}'\right)$ are associated with the creation and annihilation operators, respectively. The electron density is evaluated via

$$\begin{aligned}\rho(\vec{r},t) &= \sum_{\vec{R}\vec{R}'}\sum_{ij}\boldsymbol{\sigma}_{ij}\left(t;\vec{R}\right)\left[\chi_i\left(\vec{r}-\vec{R}'\right)\right]^*\chi_j\left(\vec{r}-\vec{R}-\vec{R}'\right)\\ &= \frac{1}{\Omega_{BZ}}\int d\vec{k}\boldsymbol{\sigma}_{ij}^{\vec{k}}(t)\left[\phi_i^{\vec{k}}(\vec{r})\right]^*\phi_j^{\vec{k}}(\vec{r}).\end{aligned} \tag{7.3}$$

Here, the Bloch functions $\phi_i^{\vec{k}}(\vec{r}) = \sum_{\vec{R}}\chi_i\left(\vec{r}-\vec{R}\right)e^{i\vec{k}\vec{R}}$ assume the same periodicity as the lattice, and Ω_{BZ} is the volume of the Brillouin zone.

For open systems, a general Kohn–Sham EOM is [18]

$$i\dot{\boldsymbol{\sigma}}(t) = [\boldsymbol{h}(t),\boldsymbol{\sigma}(t)] - i\,\boldsymbol{Q}(t). \tag{7.4}$$

Here, both $\boldsymbol{h}(t)$ and $\boldsymbol{\sigma}(t)$ have the size of the open system D, and the matrix $\boldsymbol{Q}(t)$ addresses the influences of the environment and the dissipative processes occurring at the open boundary surrounding the region D. In particular, $I(t) = -tr\left[\boldsymbol{Q}(t)\right]$ gives the total electron current flowing over the boundary at time t. We can say that (7.4) is self-closed, according to the TD-HEDT. Because all physical quantities are explicit or implicit functional of $\rho_D(\vec{r},t)$. In principle, the dissipation term $\boldsymbol{Q}(t)$ depends only on $\rho_D(\vec{r},t)$, while in practice, information about the environment is crucially useful for accurate characterization of the dissipative processes.

(II) **Evaluation of dissipation functional $\boldsymbol{Q}(t)$**

The biggest challenge in developing a practical TDDFT-OS method is to find an accurate and efficient scheme to compute $\boldsymbol{Q}(t)$. A number of approaches have been proposed, such as the non-equilibrium Green's function (NEGF) method [36, 37], the adiabatic wide-band limit approximation (AWBL) [18], and the perturbative master equation approach [38, 39]. The practicality of these approaches is restrained by their respective limitations. For instance, in the TDDFT-NEGF formalism, (7.4) becomes an integro-differential equation which is nearly impossible to solve [18]. Although the AWBL approximation simplifies the computation of $\boldsymbol{Q}(t)$, the resulting electronic dynamics is sometimes not accurate enough if the external driving field has a large amplitude or a high frequency.

In the NEGF formalism, the effects of environment are characterized by the self-energies. At equilibrium, the self-energies are

$$\begin{aligned}\tilde{\boldsymbol{\Sigma}}^{<}(t) &= i\int \mathrm{d}\epsilon f_\beta(\epsilon)\boldsymbol{\Lambda}(\epsilon)e^{-i\epsilon t}\\ \tilde{\boldsymbol{\Sigma}}^{>}(t) &= -i\int \mathrm{d}\epsilon\left[1-f_\beta(\epsilon)\right]\boldsymbol{\Lambda}(\epsilon)e^{-i\epsilon t},\end{aligned} \tag{7.5}$$

where $f_\beta(\epsilon)$ is the Fermi function with $\beta = 1/k_B T$ and $\mathbf{\Lambda}(\epsilon)$ is the spectral function (or linewidth) matrix of the environment.

Then, the dissipation functional corresponding to the αth reservoir, $\boldsymbol{Q_\alpha}(t)$, is expressed as

$$\boldsymbol{Q_\alpha}(t) = -\int_{-\infty}^{t} \mathrm{d}\tau \big[\boldsymbol{G}^r(t,\tau)\mathbf{\Sigma}_\alpha^<(\tau,t) + \boldsymbol{G}^<(t,\tau)\mathbf{\Sigma}_\alpha^a(\tau,t) + \mathrm{H.c.}\big]. \tag{7.6}$$

Here, $G^x(t,\tau)$ with $x \equiv r, a, \langle, \rangle$ are the non-equilibrium Green's functions of the open system D, $\mathbf{\Sigma}_\alpha^x(\tau,t)$ are the self-energies corresponding to the αth reservoir and $\boldsymbol{Q}(t) = \sum_\alpha \boldsymbol{Q_\alpha}(t)$. The Green's functions are then obtained by solving their EOM as follows:

$$\begin{aligned} i\tfrac{\partial}{\partial t}\boldsymbol{G}^r(t,\tau) &= \delta(t-\tau)\boldsymbol{I} + \boldsymbol{h}(t)\boldsymbol{G}^r(t,\tau) + \int_{-\infty}^{\infty} \mathrm{d}t_1 \mathbf{\Sigma}^r(t,t_1)\boldsymbol{G}^r(t_1,\tau) \\ i\tfrac{\partial}{\partial t}\boldsymbol{G}^<(t,\tau) &= \boldsymbol{h}(t)\boldsymbol{G}^<(t,\tau) + \int_{-\infty}^{\infty} \mathrm{d}t_1 \big[\mathbf{\Sigma}^<(t,t_1)\boldsymbol{G}^a(t_1,\tau) + \mathbf{\Sigma}^r(t,t_1)\boldsymbol{G}^<(t_1,\tau)\big] \end{aligned}. \tag{7.7}$$

Here, $\mathbf{\Sigma}^x(t,t_1) = \sum_\alpha \mathbf{\Sigma}_\alpha^x(\tau,t)$. With the knowledge of $\mathbf{\Sigma}_\alpha^x(\tau,t)$, (7.6) and (7.7) provide a practical scheme for the evaluation of dissipation functional $\boldsymbol{Q}(t)$. In the non-equilibrium situation where a homogeneous time-dependent potential is applied to the αth reservoir, the chemical potential of αth reservoir is shifted from its equilibrium value by $\Delta\mu_\alpha(t)$. This breaks the translational invariance of self-energies in time as follows:

$$\mathbf{\Sigma}_\alpha^x(\tau,t) = e^{-i\int_\tau^t \Delta\mu_\alpha(t_1)\mathrm{d}t_1}\tilde{\mathbf{\Sigma}}_\alpha^x(t-\tau). \tag{7.8}$$

The NEGF formalism has been employed to study time-dependent electron transport [37]. Note that (7.4) is an integro-differential equation with $\boldsymbol{Q}(t)$ expressed by (7.6), which makes the numerical implementation very difficult. To simplify numerical calculations, approximate schemes based on (7.6) have been developed. For example, the AWBL approximation we discussed above. The wide-band limit essentially neglects the energy dependence of reservoir spectral function, and thus, the integration on the right-hand side of (7.6) can be performed analytically. The adiabatic approximation further simplifies the memory of Green's functions [36]. The AWBL approximation can reduce the complexity and the computational cost associated with the TDDFT-NEGF approach. The AWBL scheme has been successfully applied to simulate the real-time electron transport in carbon nanotube-based nanoelectronic devices. However, when the external perturbation involves high-frequency components, one must always be careful about the AWBL results [40], particularly for the adiabatic approximation which may no longer be valid, or when the amplitude of perturbation is significantly larger than the system-reservoir coupling strength,

since the energy dependence of reservoir spectral function may become critical to the dynamics of open system.

(III) **TDDFT-HEOM for an open system**

In recent years, we have developed a quantum dissipation theory—the hierarchical equations of motion (HEOM) theory for general open electronic systems [41, 42]. The HEOM method works for the characterization of both equilibrium and non-equilibrium as well as static and dynamic properties [43–48]. The HEOM formalism resolves non-perturbatively the combined effects of electron–electron interaction, system–environment dissipative coupling, and non-Markovian memory. The basic variables of the HEOM are the reduced system density matrix and a number of auxiliary density matrices. For electron–electron interaction systems, the hierarchy needs to be truncated at a certain level L. Mathematically, this can be done by setting all the auxiliary density matrices at the levels higher than L to zero. In theory, the exact solution is guaranteed at $L \to \infty$, provided that the environment satisfies the Gaussian statistics. In practice, the results usually converge rapidly with the increasing L at finite temperatures. Once the convergence is achieved, the numerical outcome is considered to be quantitatively accurate [46].

For non-interacting electronic systems, it is important to notice that the HEOM formalism has a remarkable feature—the hierarchy terminates automatically at $L = 2$ without approximation [41]. This has been verified by numerous calculations. Noting that the Kohn–Sham reference system is effectively non-interacting, it is thus ideal to integrate the HEOM approach into the framework of TDDFT. In this way, a TDDFT-HEOM approach can be developed to describe realistic open electronic systems [49–52].

The TDDFT-HEOM formalism is formally equivalent to the TDDFT-NEGF method [49], and it is numerically much more convenient. Because the integro-differential equation associated with the NEGF method is now replaced by a set of differential equations, which can be solved straightforwardly.

The construction of HEOM depends on how the self-energies $\tilde{\Sigma}^{<}(t)$ and $\tilde{\Sigma}^{>}(t)$ are expanded into exponential functions. In the context of quantum dissipation theory, this means what characteristic modes one uses to resolve the memory of environment. Mathematically, this can be achieved by applying the contour integral technique with the residual theorem [41, 53]. In this way, the poles of both $f_\beta(\epsilon)$ and $\mathbf{\Lambda}(\epsilon)$ in the complex energy space contribute to the resulting characteristic memory modes. Various schemes have been proposed for the decomposition of memory, such as the Matsubara decomposition scheme [41], the partial fractional decomposition scheme [54], a hybrid Matsubara decomposition and frequency dispersion scheme [53], and a Padé decomposition scheme [55–57]. Among all these schemes, the Padé decomposition scheme is so far the most efficient one [42].

(i) **TDDFT-NEGF based on a Padé and Lorentzian decomposition scheme**

To resolve the spectral function of a realistic bulk material, we use a combined Padé and Lorentzian decomposition (PLD) scheme [49, 50], which involves the following

expansions:

$$f_\alpha(\epsilon) = \frac{1}{e^{\beta(\epsilon-\mu)}+1} \approx \frac{1}{2} + \sum_{P=1}^{P} \frac{R_P}{\beta}\left(\frac{1}{\epsilon - \mu - \frac{z_P^+}{\beta}} + \frac{1}{\epsilon - \mu - \frac{z_P^-}{\beta}}\right), \tag{7.9}$$

$$\mathbf{\Lambda}(\epsilon) \approx \sum_{d=1}^{D} \frac{1}{(\epsilon - \Omega_d)^2 + W_d^2}\mathbf{\Lambda_d}. \tag{7.10}$$

Here, μ is environment chemical potential at equilibrium. The weights $\{R_P\}$ and poles $\left\{z_P^\pm\right\}$ are determined by Padé expansion [56]. In principle, the expansion of (7.9) becomes exact at $P \to \infty$. In practice, the value of P must be sufficiently large to preserve the accuracy of (7.9), but not too large to reduce the computational cost for the HEOM. For instance, at $T = 100$ K, a minimal $P = 20$ is required to reproduce $f_\beta(\epsilon)$ accurately. As the temperature lowers, a larger P is needed. In (7.10), $\{\Omega_d\}$ and $\{W_d\}$ are the centers and widths of the Lorentzian functions, and $\{\mathbf{\Lambda_d}\}$ are the coefficient matrices. They are obtained by a least-square fit to $\mathbf{\Lambda}(\epsilon)$. The Lorentzian fitting of $\mathbf{\Lambda}(\epsilon)$ is not unique, and the strategy of finding the optimal $\{\Omega_d\}$ and $\{W_d\}$ varies from system to system.

By inserting (7.9) and (7.10) into (7.5), and using the contour integral technique as well as the residue theorem, the greater and lesser self-energies are expanded as

$$\tilde{\mathbf{\Sigma}}^x(t) \cong \sum_{m=1}^{M} \tilde{\mathbf{\Sigma}}_m^x(t) = \sum_{m=1}^{M} \boldsymbol{A}_m^{x,\sigma} e^{\gamma_m^\sigma t}. \tag{7.11}$$

With $M = P + D$ and $\sigma = \pm$. Each component of self-energy $\tilde{\mathbf{\Sigma}}_m^x(t)$ corresponds to an exponentially decaying function of $|t|$, and it is associated with the characteristic memory time $\left|\mathrm{Re}\left(\gamma_m^\sigma\right)\right|^{-1}$. The coefficients $\left\{\boldsymbol{A}_m^{x,\sigma}\right\}$ and $\left\{\gamma_m^\sigma\right\}$ are evaluated via

$$\boldsymbol{A}_m^{<,\pm} = \begin{cases} \frac{i\pi\mathbf{\Lambda_m}}{W_m} f_\beta(\Omega_m \pm i W_m) & m \le D \\ \mp\frac{2\pi R_P}{\beta}\mathbf{\Lambda}\left(\mu + \frac{z_P^\pm}{\beta}\right) & m > D,\ p = m - D \end{cases},$$

$$\boldsymbol{A}_m^{>,\pm} = \begin{cases} -\frac{i\pi\mathbf{\Lambda_m}}{W_m}(1 - f_\beta)(\Omega_m \pm i W_m) & m \le D \\ \mp\frac{2\pi R_P}{\beta}\mathbf{\Lambda}\left(\mu + \frac{z_P^\pm}{\beta}\right) & m > D,\ p = m - D \end{cases},$$

$$\gamma_m^\pm = \begin{cases} -i(\Omega_m \pm i W_m) & m \le D \\ -i\left(\mu + \frac{z_P^\pm}{\beta}\right) & m > D,\ p = m - D \end{cases}. \tag{7.12}$$

Equation (7.11) holds only at $t > 0$ with $\sigma = -$, while it is valid only at $t < 0$ with $\sigma = +$.

Based on the PLD scheme, the TDDFT-HEOM is established as follows:

$$i\dot{\boldsymbol{\sigma}}(t) = [\boldsymbol{h}(t), \boldsymbol{\sigma}(t)] - \sum_{m=1}^{M}\left[\boldsymbol{\varphi}_m(t) - \boldsymbol{\varphi}_m^{\dagger}\right], \tag{7.13}$$

$$\begin{aligned} i\dot{\boldsymbol{\varphi}}_m(t) = &\left[\boldsymbol{h}(t) - \Delta\mu(t) - i\gamma_m^{+}\right]\boldsymbol{\varphi}_m(t) + \sum_{m'=1}^{M}\boldsymbol{\psi}_{mm'}(t) \\ &- i\left[(I - \boldsymbol{\sigma}(t))\boldsymbol{A}_m^{<,+} + \boldsymbol{\sigma}(t)\boldsymbol{A}_m^{>,+}\right], \end{aligned} \tag{7.14}$$

$$\begin{aligned} i\dot{\boldsymbol{\psi}}_{mm'}(t) = &i\left(\gamma_{m'}^{-} - \gamma_m^{+}\right)\boldsymbol{\psi}_{mm'}(t) + i\left(\boldsymbol{A}_{m'}^{>,-} - \boldsymbol{A}_{m'}^{<,-}\right)\boldsymbol{\varphi}_m(t) \\ &- i\boldsymbol{\varphi}_{m'}^{\dagger}(t)\left(\boldsymbol{A}_m^{>,+} - \boldsymbol{A}_m^{<,+}\right). \end{aligned} \tag{7.15}$$

Here, $\{\boldsymbol{\varphi}_m(t)\}$ are the first-level auxiliary density matrices, and their definitions depend on how the self-energies originating from the system–reservoir couplings are decomposed into modes of different characteristic dissipation time scales. $\{\boldsymbol{\psi}_{mm'}(t)\}$ are the second-level auxiliary density matrices. Obviously, (7.4), (7.11)–(7.15) form a closed set of equations for the dynamical variables $\{\boldsymbol{\sigma}(t), \boldsymbol{\varphi}_m(t), \boldsymbol{\psi}_{mm'}(t)\}$, which determine completely the real-time dynamics of the open system, and the total number of unknown matrices is $M^2 + M + 1$ with $M = P + D$.

The equilibrium or non-equilibrium steady states of the open system can be readily achieved by setting all the time derivatives [the left-hand sides of (7.4), (7.14), and (7.15)] to zero. The stationary values of dynamical variables are thus obtained by solving the resulted linear problem for $\{\boldsymbol{\sigma}(t), \boldsymbol{\varphi}_m(t), \boldsymbol{\psi}_{mm'}(t)\}$.

(ii) **TDDFT-NEGF based on a Padé and squared-Lorentzian decomposition scheme**

To preserve the positive semi-definiteness of $\boldsymbol{\Lambda}(\epsilon)$, we replace the Lorentzian expansion of (7.10) by the following decomposition: [58]

$$\boldsymbol{\Lambda}(\epsilon) \approx \hat{\Lambda}(\epsilon) = \boldsymbol{L}^{\boldsymbol{t}}(\epsilon)\boldsymbol{L}(\epsilon), \tag{7.16}$$

$$\boldsymbol{L}(\epsilon) = \sum_{d=1}^{D}\frac{1}{(\epsilon - \Omega_d)^2 + W_d^2}\boldsymbol{L}_{\boldsymbol{d}}. \tag{7.17}$$

$\boldsymbol{L}^{\boldsymbol{t}}(\epsilon)$ denotes the transpose of the auxiliary matrix $\boldsymbol{L}(\epsilon)$. Here, we expand $\boldsymbol{L}(\epsilon)$ rather than $\hat{\Lambda}(\epsilon)$ by Lorentzian basis functions, with Ω_d (W_d) being the center (width) of dth Lorentzian function and $\boldsymbol{L}_{\boldsymbol{d}}$ the corresponding coefficient matrix.

The square form of (7.16) is to ensure that all eigenvalues of the fitted reservoir spectral matrix $\hat{\Lambda}(\epsilon)$ are non-negative at any ϵ. Hence, (7.9), (7.16), and (7.17) constitute a combined PSLD scheme, with which the equilibrium self-energies $\tilde{\boldsymbol{\Sigma}}^{x}(t)$ are expanded as follows:

$$\tilde{\boldsymbol{\Sigma}}^{x}(t) \cong \begin{cases} \sum_{m=1}^{M} \boldsymbol{A}_m^{x,+} e^{-i\gamma_m^{+}t} + \sum_{d=1}^{D} \boldsymbol{A}_d^{x,+} e^{-i\gamma_d^{+}t} \\ \sum_{m=1}^{M} \boldsymbol{A}_m^{x,-} e^{-i\gamma_m^{-}t} + \sum_{d=1}^{D} \boldsymbol{A}_d^{x,-} e^{-i\gamma_d^{-}t} \end{cases}. \tag{7.18}$$

The Padé and squared-Lorentzian decomposition (PSLD) scheme gives rise to additional polynomial exponential memory components that are proportional to $te^{-i\gamma_d^{\pm}t}$. These new components originate from the second-order poles of $\hat{\Lambda}(\epsilon)$ given by (7.16). Note that the time derivative of a polynomial exponential function $t^n e^{\gamma t}$ only involves polynomial exponentials of lower orders. Therefore, a set of formally closed HEOM can be constructed based on (7.18). In fact, the polynomial exponential type of reservoir memory function has been adopted to construct a hierarchical set of quantum dynamics equations for studying the dissipative dynamics of a spin-boson model.

The PSLD scheme needs three types of the first-tier auxiliary density matrices and nine types of the second-tier auxiliary density matrices; the derivation process is similar to the PLD scheme. Therefore, for the same system, the TDDFT-NEGF constructed based on the PSLD scheme requires about nine times of memory as that of the PLD counterpart. But the new TDDFT-NEGF established with the squared-Lorentzian decomposition of $\hat{\Lambda}(\epsilon)$ is quantitatively accurate and numerically much more stable than the HEOM constructed by using the PLD scheme.

(iii) **TDDFT-NEGF based on a Padé and complex absorbing potential scheme**

By imposing an absorption potential in finite region on the boundary, the complex absorbing potential (CAP) is an artificial potential, which mimics the infinite environment. The commonly used CAP is derived from the semi-classical approximation by minimizing the reflection coefficient in a 1D quantum wave system [59]. This potential increases from zero on one side of the CAP region near the device to infinity near another side. The blue curve in Fig. 7.3 shows the profile of the CAP. One most used CAP has the following form:

$$W(x) = i\frac{\hbar^2}{2m}\left(\frac{2\pi}{\Delta x}\right)^2 f(x). \tag{7.19}$$

Here, $f(x) = \frac{4}{c^2}\left[\left(\frac{\Delta x}{x_2 - 2x_1 + x}\right)^2 + \left(\frac{\Delta x}{x_2 - x}\right)^2 - 2\right]$, x_1, and x_2 are the beginning and end position of the CAP region, and $\Delta x = x_2 - x_1$ is the length of this region. c is an insensitive constant to the final result unless it is too large or too small (one can just set c = 1.0 to make the case easier in some circumstances). When the CAP is used for the atomic transport system, a series of repeated blocks of the lead units (in x direction) constitute the CAP region, as shown in Fig. 7.3. It is noted that the parameters entailing the details of the lead electron are involved in the Hamiltonian of repeated units, which are not exhibited in the CAP expression; see (7.19). After projecting the CAP expression into the atomic basis $\{\phi_n(x, y, z)\}$, the following

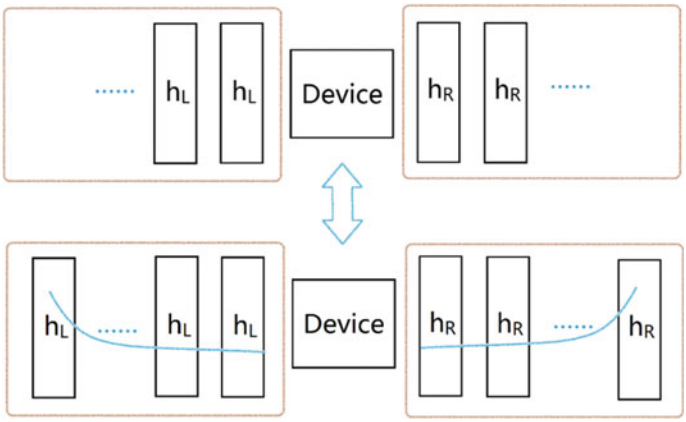

Fig. 7.3 The demonstration of the CAP method. The upper part shows the common transport case and the lower part shows the CAP scheme f or such transport calculation. In the upper part, the left and right lead regions contain infinite repeated units; in the lower part, the two CAP regions with finite repeated units can mimic the two semi-infinite leads. The complex potentials (imaginary part) in the CAP regions are indicated by two blue curves

CAP matrix is obtained:

$$W_{\alpha,mn} = \int \phi_m^*(x, y, z) W_\alpha(x) \phi_n(x, y, z) dx dy dz. \tag{7.20}$$

The CAP can mimic the infinite leads, and the calculated physical property of the device region (or the device portion of G^r_{CAP}) is very close to that calculated from the NEGF theory (or G^r_D). But the lead portions of G^r_{CAP} have no such correspondence with the lead regions in the open system. Only in the positions very close to the device, $G^r(\epsilon)$ of the two systems have close values. The correspondence in two systems is shown in Fig. 7.3. The upper panel shows an open system with device and two sets of leads with infinite units (with the Hamiltonian h_L or h_R); the lower panel shows the device region and two CAP regions with finite units. The imaginary part of CAP is demonstrated by the blue curve. It is worth to note that W_α is energy independent, which is much easier to be evaluated than the iterative calculation of $\Sigma^r(\epsilon)$.

Since the CAP is energy independent, we may write the Green's function with CAP into the spectrum form,

$$G^r_{m,n} = \sum_k \frac{\psi_{m,k} \Phi^*_{n,k}}{\epsilon - \epsilon_k}, \tag{7.21}$$

where $G^r_{m,n} = \phi_m(\vec{r}) | G^r(\vec{r}, \vec{r}') | \phi_n(\vec{r}\prime)$, $\psi_{m,k} = \phi_m(\vec{r}) | \psi_k(\vec{r})$, $\Phi^*_{n,k} = \Phi^*_k(\vec{r}\prime) | \phi_n(\vec{r}\prime)$, and

$$\left(H_0 + \sum_{\alpha=L,R} W_\alpha\right)\psi_k(\vec{r}) = \epsilon_k \psi_k(\vec{r}), \tag{7.22}$$

$$\left(H_0 + \sum_{\alpha=L,R} W_\alpha^\dagger\right)\Phi_k^*(\vec{r}) = \epsilon_k^* \Phi_k^*(\vec{r}). \tag{7.23}$$

As the eigenvalue ϵ_k is a complex number, it is natural to consider that (7.21) has some Lorentzian expansion form. To see this, we write the numerator and ϵ_k into the real and imaginary parts: $\psi_{m,k}\Phi_{n,k}^* = A_{k,mn}^R + iA_{k,mn}^I$ and $\epsilon_k = \Omega_k + iW_k$, then we have

$$G_{m,n}^r = \sum_k \frac{\left(A_{k,mn}^R + iA_{k,mn}^I\right)(\epsilon - \Omega_k + iW_k)}{(\epsilon - \Omega_k + iW_k)(\epsilon - \Omega_k - iW_k)} = \sum_k \frac{B_{k,mn}^R + iB_{k,mn}^I}{(\epsilon - \Omega_k)^2 + W_k^2}. \tag{7.24}$$

It is easy to prove that the self-energy matrix can be written into such Lorentzian form as well [60]. We see that this Lorentzian form has a little difference from the standard one, but after some modifications, it can be used for the residue calculations, and TDDFT-NEGF can be implemented like PLD.

(iv) **Initial values for TDDFT-HEOM**

It is important to find the proper initial values for RSDM, first- and second-tier ARSDM [61], which are essential for the propagation of HEOM to produce physically correct results. The system is assumed to be initially in the equilibrium state. The first- and second-tier ARSDM keep unchanged for the steady state of the system (i.e., $\dot{\sigma}_D = \dot{\varphi}_{\alpha,k} = \dot{\varphi}_{\alpha,k,\alpha',k'} = 0$). And the electrons occupy the single-particle states according to the Fermi–Dirac distribution. The equilibrium RSDM can be calculated by a semi-circular contour integral of $G_D^r(\epsilon)$ on the upper complex plane,

$$\begin{aligned}\sigma_D^{eq} &= -\frac{1}{\pi}\mathrm{Im}\left[\int_{-\infty}^{+\infty} \mathrm{d}\epsilon f\epsilon(\epsilon - \mu)G_D^r(\epsilon)\right] \\ &= -\frac{1}{\pi}\mathrm{Im}\left[\int_C \mathrm{d}\epsilon f(\epsilon - \mu)G_D^r(\epsilon) + \sum_p R_p G_D^r(\zeta_p)\right],\end{aligned} \tag{7.25}$$

where C is a semi-circular contour on the upper complex plane and $\zeta_p = \mu + iz_p$ and $-R_p$ are the pth Padè pole and residue of the Fermi function. The summation runs through all singularities lying between the semi-circle and real axis.

The equilibrium-state first-tier ARSDM can be evaluated by the residue theorem since the semi-circle contour integral trends to zero when its radius trends to infinity,

$$\varphi_{\alpha k} = -G_D^r(\epsilon_\alpha)\left[iA_{\alpha k}^{<+} + f(\epsilon_\alpha - \mu)\Lambda_{\alpha k}\right] - 2\sum_{p=1}^{N_p}[\epsilon_\alpha^* \mathrm{Re}\left(\Xi_{\alpha kp}\right) - \mathrm{Re}\left(\zeta_p \Xi_{\alpha kp}\right)]\Lambda_{\alpha k}, \tag{7.26}$$

where $\Xi_{\alpha kp} = \frac{R_p}{(\zeta_p - \alpha)(\zeta_p - \epsilon_\alpha^*)} G_D^r(\zeta_p)$, and once the first-tier ARSDM are known, initial values for second tier ARSDM $\varphi_{\alpha,k,\alpha',k'}$ can be evaluated directly by requiring them to satisfy $\dot{\varphi}_{\alpha,k,\alpha',k'} = 0$. This gives

$$\varphi_{\alpha k,\alpha' k'} = \frac{\Lambda_{\alpha' k'}\varphi_{\alpha k} - \varphi_{\alpha' k'}^{\dagger}\Lambda_{\alpha k}}{\epsilon_\alpha - \epsilon_\alpha^*}. \tag{7.27}$$

With the proper initial values for σ_D^{eq}, $\varphi_{\alpha k}$ and $\varphi_{\alpha k,\alpha' k'}$, we can propagate the HEOM to obtain the time-dependent $\sigma_D(t)$, $\varphi_{\alpha k}(t)$, and $\varphi_{\alpha k,\alpha' k'}(t)$.

7.3 Results and Discussions

7.3.1 *Real-Time Electron Transport in Quasi-One-Dimensional Atomic Chains*

By using the TDDFT-HEOM approach, we present numerical simulations on the real-time electron transport through quasi-one-dimensional atomic chains in this subsection. Figure 7.4 demonstrates the system considered, where the system (region D) consists of m layers of atoms, and all layers are of width *n*. For simplicity, the atomic chain is described by the tight-binding model Hamiltonian with the on-site energy $\epsilon_0 = 0$ and nearest-neighbor coupling $\gamma = 1$ eV.

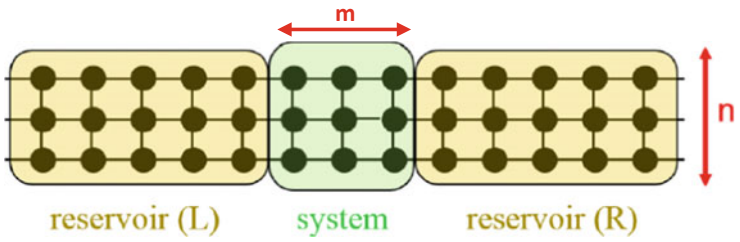

Fig. 7.4 Schematic diagram of a quasi-1D atomic chain with a finite width *n*. Within the framework of TDDFT-OS, the green region is taken as the (open) system, and the yellow regions are treated as electron reservoirs (the environment) for the system. Reprinted with permission from [58]. Copyright 2015, AIP Publishing LLC

Firstly, we verify the accuracy of self-energy decomposition of (7.11). By examining the projected density of states (PDOS) of the open system D at equilibrium, we have that

$$N_D(\epsilon) = -\frac{1}{\pi}\mathrm{Im}\left\{\mathrm{tr}\left[\epsilon - \boldsymbol{h} - \tilde{\boldsymbol{\Sigma}}^r(\epsilon)\right]^{-1}\right\}. \tag{7.28}$$

Here, $\tilde{\boldsymbol{\Sigma}}^r(\epsilon) = \sum_\alpha \tilde{\Sigma}^r_\alpha(\epsilon) = \boldsymbol{\Gamma}(\epsilon) - i\boldsymbol{\Lambda}(\epsilon)$ is the equilibrium retarded self-energy arising from the system-reservoir couplings, and $\boldsymbol{\Gamma}(\epsilon)$ is deduced from $\boldsymbol{\Lambda}(\epsilon) = \sum_\alpha \boldsymbol{\Lambda}_{\boldsymbol{\alpha}}(\epsilon)$ via the Kramers–Kronig relation [62]. A renormalization approach [63] utilizing the translational symmetry along the chain axis is employed, which yields highly accurate $\tilde{\Sigma}^r_\alpha(\epsilon)$ and $\boldsymbol{\Lambda}_{\boldsymbol{\alpha}}(\epsilon)$. Using the Lorentzian decomposition of (7.10), with a total number of 45 Lorentzian functions, the fitted $\tilde{\Sigma}^r_\alpha(\epsilon)$ and $\boldsymbol{\Lambda}_{\boldsymbol{\alpha}}(\epsilon)$ are obtained, and then, the corresponding PDOS of the system is evaluated through (7.28).

Initially, the entire chain is in its equilibrium at the temperature $T = 100$ K. Figure 7.5 shows that the PDOS calculated with the two approaches is found to agree very well with each other for all the systems studied. The van Hove singularities are only trivially broadened. Such a comparison clearly affirms that the present self-energy decomposition can reproduce very accurately the electronic structure of the open system.

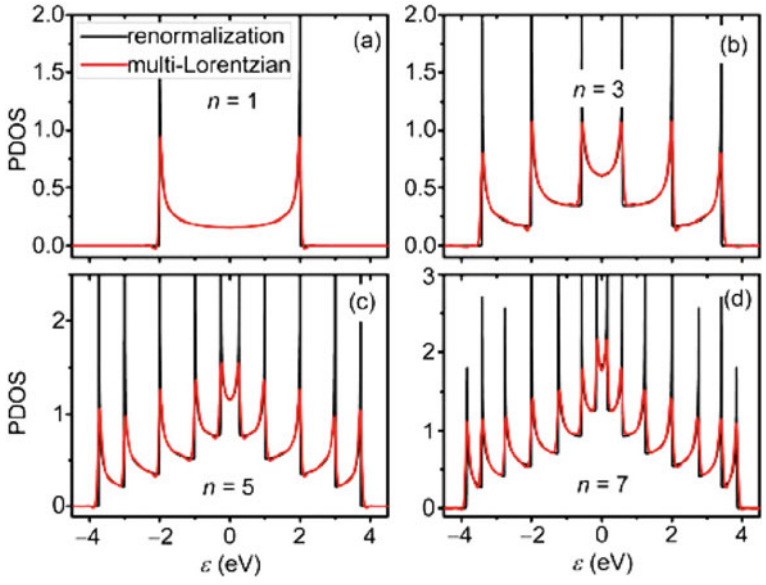

Fig. 7.5 Calculated equilibrium $N_D(\epsilon)$ for atomic chains of width **a** $n = 1$, **b** $n = 3$, **c** $n = 5$, and **c** $n = 7$. The system D consists of one layer ($m = 1$) of atoms in all four cases. Reprinted with permission from [16]. Copyright 2013, Science China Press and Springer-Verlag Berlin Heidelberg

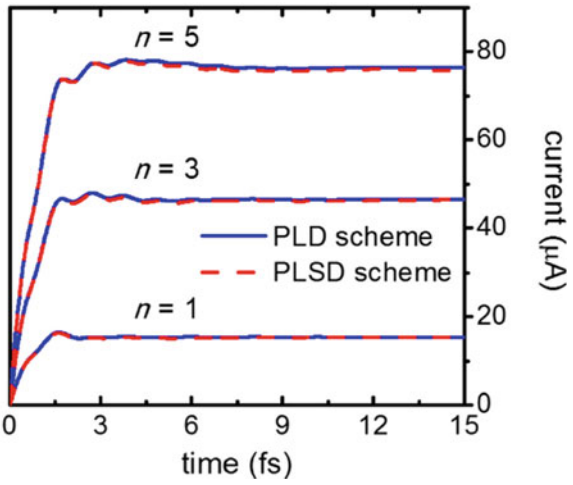

Fig. 7.6 Time-dependent currents through atomic chains of different widths ($n = 1, 3, 5$) in response to a switch-on voltage of amplitude $V_L = -V_R = 0.1$ V. The blue and red lines are obtained from the TDDFT-NEGF constructed based on the PLD and PSLD schemes, respectively. Reprinted with permission from [58]. Copyright 2015, AIP Publishing LLC

We then investigate the time-dependent electron transport through atomic chains of different widths n, assuming a bias voltage is applied across the system region. The time-dependent response current flowing through the α-reservoir is calculated by [18]

$$I_\alpha = -\mathrm{tr}\ \big[\boldsymbol{Q}_\alpha(t)\big], \tag{7.29}$$

where $\boldsymbol{Q}_\alpha(t)$ is the dissipative term defined by (7.6), or another form $\boldsymbol{Q}_\alpha(t) = -i\big[\boldsymbol{\varphi}_\alpha(t) - \boldsymbol{\varphi}_\alpha^\dagger\big]$, which comes from comparing the (7.4) and (7.13). The time-dependent response currents calculated with the TDDFT-NEGF constructed based on both the PLD and PSLD schemes are shown in Fig. 7.6.

The bias voltages are symmetrically applied to the two reservoirs, at a certain time t (set as zero), i.e.,$V_L = -V_R = V_0\Theta(t)$, with $\Theta(t)$ being a step function and $V_0 = 0.1$V. Region D is always assumed to maintain a voltage drop of $2V_0$, and we calculate the dynamic electronic response of the system D by propagating the HEOM of (7.13)–(7.15), from which the time-dependent current through the interface between D and L (or R) is obtained.

The calculated time-dependent current through a series of systems of different m and n is displayed in Fig. 7.7. All these results are expected to be quantitatively accurate. Apparently, by increasing either n or m, the system D is enlarged, and the transient response current varies more smoothly in time. This indicates that the system with a larger number of degrees of freedom behaves more classically.

(B) **Real-time electron dynamics on a two-dimensional graphene surface**

TDDFT methods have been employed to study the ultrafast electron transfer in interfacial systems, such as dye-sensitized solar cells, by using the isolated [64] and periodic [65, 66] system models. In these circumstances, the simulation results must

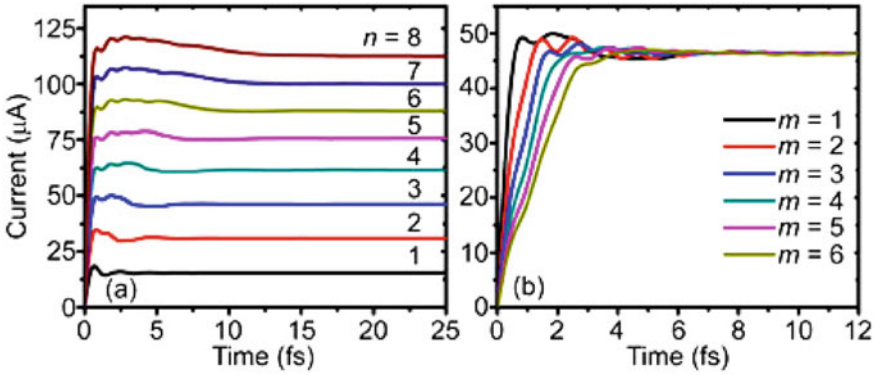

Fig. 7.7 Time-dependent response current $I(t) = I_R(t) = -I_L(t)$ under step-function bias voltages of $V_L = -V_R = V_0\Theta(t)$ with $V_0 = 0.1$ V, for systems of **a** $m = 1$ with different widths n, and **b** $n = 3$ with different numbers of layers m. The temperature is $T = 100$ K. Reprinted with permission from [16]. Copyright 2013, Science China Press and Springer-Verlag Berlin Heidelberg

be interpreted very carefully, particularly in the long-time regime. Because in real situations, a transferred electron ultimately drains into the bulk material; therefore, the number of electrons in the interfacial region is not conserved. Hence, because an open-system approach is capable of addressing exchange of electrons with the reservoir, it would be most appropriate to address the dynamic electron transfer problem.

TDDFT-OS had rarely been applied to two- or higher-dimensional systems. One of the difficulties was the accurate evaluation of reservoir spectral functions. To tackle this problem, we consider a super cell which consists of a number of unit cells [67], so that itself is still a repeating unit of the 2D lattice, and nontrivial interaction exists only between nearest-neighboring super cells.

The graphene is periodic in 2D real space. The home super cell is located at $\vec{R}_0$, and the displacement vector between two super cells is $\vec{R}$. Consider nonzero overlap integrals between two separated super cells. The surface retarded Green's function, $\boldsymbol{G}^r_{\vec{R}_0}\left(\vec{R}_1, \vec{R}_2; \epsilon\right)$, should satisfy the following equations for all combinations of $\left(\vec{R}_1, \vec{R}_2\right)$ [66]:

$$\begin{aligned}
&\sum_{\vec{R}'}\left[(\epsilon + i\eta)\boldsymbol{S}_{\vec{R}\vec{R}'} - \boldsymbol{H}_{\vec{R}\vec{R}'}\right]\boldsymbol{G}^r_{\vec{R}_0}\left(\vec{R}', \vec{R} + \overrightarrow{\vec{R}}; \epsilon\right) = \delta\left(\overrightarrow{\vec{R}}\right)\left[I - \delta\left(\vec{R} - \vec{R}_0\right)\right], \\
&\sum_{\vec{R}'}\boldsymbol{G}^r_{\vec{R}_0}\left(\vec{R} + \overrightarrow{\vec{R}}, \vec{R}'; \epsilon\right)\left[(\varepsilon + i\eta)\boldsymbol{S}_{\vec{R}'\vec{R}} - \boldsymbol{H}_{\vec{R}'\vec{R}}\right] = \delta\left(\overrightarrow{\vec{R}}\right)\left[I - \delta\left(\vec{R} - \vec{R}_0\right)\right].
\end{aligned} \tag{7.30}$$

Here, $\boldsymbol{S}$ is the overlap matrix, $\boldsymbol{H}$ is the effective single-electron Hamiltonian matrix, $\delta\left(\vec{X}\right) = I$, if $\vec{X} = \vec{0}$ and zero otherwise, and η is a positive infinitesimal.

The Green's function vanishes correctly at the boundary of home super cell because of the square bracket term on the right-hand side. Due to the bulk graphene's translational invariance, we denote $\boldsymbol{S}\left(\vec{R}' - \vec{R}\right) \equiv \boldsymbol{S}_{\vec{R}\vec{R}'}$ and $\boldsymbol{H}\left(\vec{R}' - \vec{R}\right) \equiv \boldsymbol{H}_{\vec{R}\vec{R}'}$. Their counterparts in the reciprocal space are

$$\begin{aligned} \boldsymbol{S}\left(\vec{K}\right) &= \sum_{\vec{R}} e^{i\vec{K}\vec{R}} \boldsymbol{S}\left(\vec{R}\right), \\ \boldsymbol{H}\left(\vec{K}\right) &= \sum_{\vec{R}} e^{i\vec{K}\vec{R}} \boldsymbol{H}\left(\vec{R}\right). \end{aligned} \tag{7.31}$$

The retarded bulk Green's function in reciprocal space is

$$\boldsymbol{G}_0^r\left(\vec{K};\epsilon\right) = \left[(\epsilon + i\eta)\boldsymbol{S}\left(\vec{K}\right) - \boldsymbol{H}\left(\vec{K}\right)\right]^{-1}. \tag{7.32}$$

Due to the translational invariance, the real-space Green's function corresponds to an inverse Fourier transform of

$$\boldsymbol{G}_0^r\left(\vec{R};\epsilon\right) = \int d\vec{K}\, \boldsymbol{G}_0^r\left(\vec{K};\epsilon\right) e^{i\vec{K}\vec{R}}, \tag{7.33}$$

which depends only on the displacement vector between two super cells.

As the effective single-electron Hamiltonian matrix of home super cell $\left(\boldsymbol{H}_{\vec{R}_0\vec{R}_0}\right)$ is modified by binding to the bridging molecule and deviates from the bulk Hamiltonian, an additional surface term $\left(\Delta\boldsymbol{G}_{\vec{R}_0}\left(\vec{R}_1, \vec{R}_2;\epsilon\right)\right)$ is needed to account for the vanishing amplitude of Green function at the boundary of home super cell. This surface term thus breaks the translational invariance of $\vec{R}_2 - \vec{R}_1$. The home super cell hence mimics a "point defect" in a perfect lattice. Altogether, we have

$$\boldsymbol{G}_{\vec{R}_0}^r\left(\vec{R}_1, \vec{R}_2;\epsilon\right) = \boldsymbol{G}_0^r\left(\vec{R}_2 - \vec{R}_1;\epsilon\right) - \Delta\boldsymbol{G}_{\vec{R}_0}\left(\vec{R}_1, \vec{R}_2;\epsilon\right), \tag{7.34}$$

$$\Delta\boldsymbol{G}_{\vec{R}_0}\left(\vec{R}_1, \vec{R}_2;\epsilon\right) = \boldsymbol{G}_0^r\left(\vec{R}_0 - \vec{R}_1;\epsilon\right)\left[\boldsymbol{G}_0^r\left(\vec{0};\epsilon\right)\right]^{-1} \times \boldsymbol{G}_0^r\left(\vec{R}_2 - \vec{R}_0;\epsilon\right), \tag{7.35}$$

which satisfy (7.30). To verify the formal equivalence of $\Delta\boldsymbol{G}_{\vec{R}_0}\left(\vec{R}_0, \vec{R}_0;\epsilon\right) = \boldsymbol{G}_0^r\left(\vec{0};\epsilon\right)$ is trivial. Apparently, $\boldsymbol{G}_{\vec{R}_0}^r\left(\vec{R}_1, \vec{R}_0;\epsilon\right) = \boldsymbol{G}_{\vec{R}_0}^r\left(\vec{R}_0, \vec{R}_2;\epsilon\right) = 0$. The boundary conditions are thus accounted for properly.

With the surface Green function, the retarded self-energy required, $\boldsymbol{\Sigma}_{\vec{R}_0\vec{R}_0}^r(\epsilon)$, is obtained via

$$\boldsymbol{\Sigma}_{\vec{R}_0\vec{R}_0}^r(\epsilon) = \sum_{\vec{R}_1 \neq \vec{R}_0} \sum_{\vec{R}_2 \neq \vec{R}_0} \tilde{\boldsymbol{H}}_{\vec{R}_0\vec{R}_1}(\epsilon) \boldsymbol{G}_{\vec{R}_0}^r\left(\vec{R}_1, \vec{R}_2;\epsilon\right) \tilde{\boldsymbol{H}}_{\vec{R}_2\vec{R}_0}(\epsilon), \tag{7.36}$$

where $\tilde{\boldsymbol{H}}_{\vec{R}_0\vec{R}_1}(\epsilon) \equiv (\epsilon + i\eta)\boldsymbol{S}_{\vec{R}_0\vec{R}_1} - \boldsymbol{H}_{\vec{R}_0\vec{R}_1}$.

With the reciprocal-space sampling approach we introduced above, we demonstrate the applicability of the TDDFT-HEOM approach to two-dimensional open systems. A numerical example will be presented, which explores the real-time dynamics of an excess electron on a graphene surface.

The whole system is a monolayer of bulk graphene, from which a rectangular piece is taken as the open system D. There is a mono-vacancy defect at the center of D (see Fig. 7.8a). The tight-binding parameters are $\epsilon_0 = 0$ and $\gamma = 2.7\,\text{eV}$. The calculated PDOS of D without of the defect is shown in Fig. 7.8b. Clearly, the $N_D(\epsilon)$ calculated by using the reciprocal-space sampling approach almost overlaps with that obtained from the multi-Lorentzian fitting scheme. The only small deviations are at the van Hove singularities at $\epsilon = \pm\gamma$ and the defect state at $\epsilon = 0$, which should have rather minor effect on the electronic dynamics.

The scenario of system dynamics is set as follows: Initially, the graphene is in its equilibrium state at $T = 100$ K. At time $t = 0$, an excess electron enters the system D through an atom closest to the vacancy. Such a local perturbation drives the graphene out of equilibrium and induces electronic response that propagates outward from the perturbed atom. This is analogous to adding a droplet into a quantum liquid, which will result in generation and spreading of electron ripples on the graphene surface. In particular, it is interesting to know how the electronic ripples would propagate in the presence of a local defect.

The real-time evolution of excess electron is shown in Fig. 7.9, where the density distributions of the excess electron $\Delta\rho(\vec{r}, t) = \rho(\vec{r}, t) - \rho^{\text{eq}}(\vec{r})$ at different time instants are visualized. By observing the result, the electron density propagates mainly through the carbon–carbon bonds. At the center of system D the density, rather than spreads over the vacancy site, moves around it. At time $t = 1.4$ fs, most of the excess electron has already dissipated away into the surrounding bulk graphene, because the boundary of D is almost transparent to the excess electron.

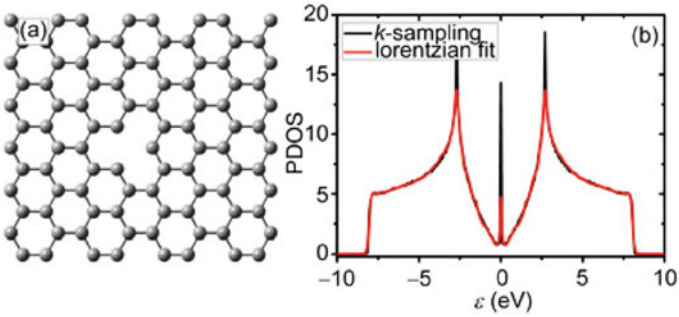

Fig. 7.8 **a** A rectangular area of a graphene monolayer with a mono-vacancy defect as the open system *D*. **b** Calculated equilibrium $N_D(\epsilon)$ of system *D* without the defect. For the two lines, the self-energies are obtained by the reciprocal-space sampling approach and from the multi-Lorentzian fitting scheme, respectively. Reprinted with permission from [16]. Copyright 2013, Science China Press and Springer-Verlag Berlin Heidelberg

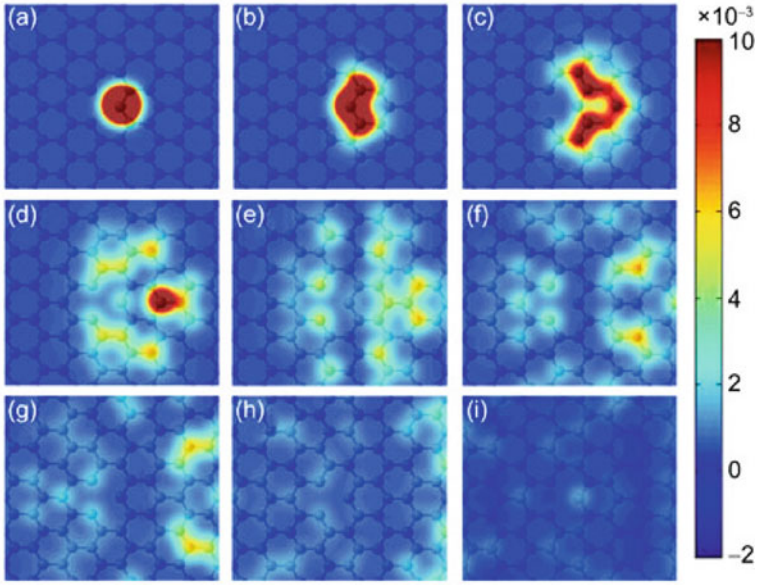

Fig. 7.9 Snapshots of time-dependent density of the excess electron in the system *D*. The panels (a–i) correspond to $t = 0$, 0.15, 0.3, 0.45, 0.6, 0.75, 0.9, 1.1, and 1.4 fs, respectively. For clear visualization, the local *pz* orbitals are represented by Gaussian functions. Reprinted with permission from [16]. Copyright 2013, Science China Press and Springer-Verlag Berlin Heidelberg

It is easily to extract some important quantities, such as the characteristic dissipation time for the excess electron, from the calculated real-time electronic dynamics. These quantities may be compared directly to experimental measurements on electronic processes on material surfaces. TDDFT-OS methods may be used to simulate these spectra and investigate the relevant ultrafast excited-state electronic dynamics at the molecule–semiconductor interfaces.

7.4 Conclusion

In conclusion, this chapter gives a comprehensive account of quantum mechanical simulation of electronic dynamics on surfaces of materials using the TDDFT-OS method. By discussing both theoretical and practical aspects, it is noted that the TDDFT-OS is based on a rigorous theoretical foundation, which is formally exact and numerically efficient with HEOM method. Firstly, the electron density inside the open system should be sufficient to determine completely and uniquely any system property in principle. Then TDDFT-OS methods have been developed practically.

As demonstrated by the numerical simulations on both one-dimensional and two-dimensional open systems, the TDDFT-HEOM approach is capable of characterizing the real-time electronic dynamics of realistic open systems.

To address more complex systems and problems, further improvement on numerical efficiency requires to enhance the practicality of TDDFT-OS. And it will make a great difference if we extend the implementation of TDDFT-HEOM from parameterized models to the first-principles level. Moreover, a more efficient and robust algorithm is in great need to resolve the reservoir memory. These progresses will lead to very promising applications in various fields of chemistry, such as energy conversion and heterogeneous catalysis.

References

1. A. Hagfeldt, M. Grätzel, Acc. Chem. Res. **33**, 269 (2000)
2. O'Regan, M. Grätzel, Nature (London) **353**, 737 (1991)
3. G. Lietal, Energy Environ. Sci. **2**, 230 (2009)
4. E. Runge, E.K.U. Gross, Phys. Rev. Lett. **52**, 997 (1984)
5. K. Burke, J. Werschnik, E.K.U. Gross, J. Chem. Phys. **123**, 062206 (2005)
6. M.K. Casida, J. Mol. Struct.: THEOCHEM **914**, 3 (2009)
7. R.E. Stratmann, G.E. Scuseria, M.J. Frisch, J. Chem. Phys. **109**, 8218 (1998)
8. R. van Leeuwen, Phys. Rev. Lett. **82**, 3863 (1999)
9. R. van Leeuwen, in *Time-Dependent Density Functional Theory*, ed. by M.A.L. Marques, C.A. Ullrich, F. Nogueira, A. Rubio, K. Burke, E.K.U. Gross, Lecture Notes in Physics, vol. 706 (Springer, Berlin, 2006), pp. 17–32
10. F. Kootstra, Ph.D. Thesis, University of Groningen (2001)
11. N.T. Maitra, I. Souza, K. Burke, Phys. Rev. B **68**, 045109 (2003)
12. R. Baer, J. Chem. Phys. **128**, 044103 (2008)
13. Y. Li, C.A. Ullrich, J. Chem. Phys. **129**, 044105 (2008)
14. C. Verdozzi, Phys. Rev. Lett. **101**, 166401 (2008)
15. Fundamentals of Time-Dependent Density Functional Theory, ed. by M.A.L. Marques, N.T. Maitra, F.M.S. Nogueira, E.K.U. Gross, A. Rubio, Lecture Notes in Physics, vol. 837 (Springer, Berlin, 2012)
16. X. Zheng, R. Wang, Sci. China Chem. **57**, 1 (2014)
17. W. Kohn, L.J. Sham, Phys. Rev. **140**, A1133–A1138 (1965)
18. X. Zheng, F. Wang, C.Y. Yam, Y. Mo, G.H. Chen, Phys. Rev. B **75**, 195127 (2007)
19. G. Stefanucci, C.O. Almbladh, Europhys. Lett. **67**, 14–20 (2004)
20. M. Di Ventra, T.N. Todorov, J. Phys. Condens. Matter **16**, 8025–8034 (2004)
21. X. Zheng, G.H. Chen, arXiv:physics/0502021
22. X. Zheng, C.Y. Yam, F. Wang, G.H. Chen, Phys. Chem. Chem. Phys. **13**, 14358–14364 (2011)
23. J. Yuen-Zhou, D.G. Tempel, C.A. Rodríguez-Rosario, A. Aspuru-Guzik, Phys. Rev. Lett. **104**, 043001 (2010)
24. D.G. Tempel, M.A. Watson, R. Olivares-Amaya, A. Aspuru-Guzik, J. Chem. Phys. **134**, 074116 (2011)
25. J. Riess, W. Münch, Theor. Chim. Acta. **58**, 295–300 (1981)
26. P.G. Mezey, Mol. Phys. **96**, 169–178 (1999)
27. S. Fournais, M. Hoffmann-Ostenhof, T. Hoffmann-Ostenhof, T.O. Sorensen, Commun. Math. Phys. **228**, 401–415 (2002)
28. S. Fournais, M. Hoffmann-Ostenhof, T. Hoffmann-Ostenhof, T.O. Sorensen, Ark. Mat. **42**, 87–106 (2004)

29. T. Jecko, Lett. Math. Phys. **93**, 73–83 (2010)
30. K. Burke, R. Car, R. Gebauer, Phys. Rev. Lett. **94**, 146803 (2005)
31. J. Yuen-Zhou, C. Rodriguez-Rosario, A. Aspuru-Guzik, Phys. Chem. Chem. Phys. **11**, 4509–4522 (2009)
32. C.Y. Yam, S. Yokojima, G.H. Chen, Phys. Rev. B **68**, 153105 (2003)
33. C.Y. Yam, S. Yokojima, G.H. Chen, J. Chem. Phys. **119**, 8794–8803 (2003)
34. M.E. Casida, *Recent Developments and Applications in Density Functional Theory* (Elsevier, Amsterdam, 1996)
35. A. Castro, H. Appel, M. Oliveira, C.A. Rozzi, X. Andrade, F. Lorenzen, M.A.L. Marques, E.K.U. Gross, A. Rubio, Phys. Stat. Sol. B **243**, 2465–2488 (2006)
36. S. Kurth, G. Stefanucci, C.O. Almbladh, A. Rubio, E.K.U. Gross, Phys. Rev. B **72**, 035308 (2005)
37. Y. Zhu, J. Maciejko, T. Ji, H. Guo, J. Wang, Phys. Rev. B **71**, 075317 (2005)
38. X.Q. Li, Y.J. Yan, Phys. Rev. B **75**, 075114 (2007)
39. P. Cui, X.Q. Li, J.S. Shao, Y.J. Yan, Phys. Lett. A **357**, 449 (2006)
40. S. Chen, H. Xie, Y. Zhang, X. Cui, G. Chen, Nanoscale **5**, 169 (2013)
41. J.S. Jin, X. Zheng, Y.J. Yan, J. Chem. Phys. **128**, 234703 (2008)
42. X. Zheng, R.X. Xu, J. Xu, J.S. Jin, J. Hu, Y.J. Yan, Prog. Chem. **24**, 1129–1152 (2012)
43. X. Zheng, J.S. Jin, Y.J. Yan, J. Chem. Phys. **129**, 184112 (2008)
44. X. Zheng, J.S. Jin, Y.J. Yan, New J. Phys. **10**, 093016 (2008)
45. X. Zheng, J.Y. Luo, J.S. Jin, Y.J. Yan, J. Chem. Phys. **130**, 124508 (2009)
46. Z.H. Li, N.H. Tong, X. Zheng, D. Hou, J.H. Wei, J. Hu, Y.J. Yan, Phys. Rev. Lett. **109**, 266403 (2012)
47. X. Zheng, Y.J. Yan, M. Di Ventra, Phys. Rev. Lett. **111**, 086601 (2013)
48. S. Wang, X. Zheng, J.S. Jin, Y.J. Yan, Phys. Rev. B **88**, 035129 (2013)
49. X. Zheng et al., J. Chem. Phys. **133**, 114101 (2010)
50. H. Xie et al., J. Chem. Phys. **137**, 044113 (2012)
51. H. Tian, G.H. Chen, J. Chem. Phys. **137**, 204114 (2012)
52. Y. Zhang, S.G. Chen, G.H. Chen, Phys. Rev. B **87**, 085110 (2013)
53. X. Zheng, J.S. Jin, S. Welack, M. Luo, Y.J. Yan, J. Chem. Phys. **130**, 164708 (2009)
54. A. Croy, U. Saalmann, Phys. Rev. B **80**, 073102 (2009)
55. T. Ozaki, Phys. Rev. B **75**, 035123 (2007)
56. J. Hu, R.X. Xu, Y.J. Yan, J. Chem. Phys. **133**, 101106 (2010)
57. J. Hu, M. Luo, F. Jiang, R.X. Xu, Y.J. Yan, J. Chem. Phys. **134**, 244106 (2011)
58. R.L. Wang, X. Zheng, Y.H. Kwok, H. Xie, G.H. Chen, C.Y. Yam, J. Chem. Phys. **142**, 144112 (2005)
59. T. Gonzalez-Lezana, E.J. Rackham, D.E. Manolopoulos, J. Chem. Phys. **120**, 2247 (2004)
60. H. Xie, Y. Kwok, F. Jiang, X, Zheng, G.H. Chen, J. Chem. Phys. **141**, 164122 (2014)
61. Y.H. Kwok, H. Xie, C.Y. Yam, X. Zheng, G.H. Chen, J. Chem. Phys. **139**, 224111 (2013)
62. J.S. Toll, Phys. Rev. **104**, 1760 (1956)
63. M.P.L. Sancho, J.M.L. Sancho, J.M.L. Sancho, J. Rubio, J. Phys. F:Met. Phys. **15**, 851 (1985)
64. Z. Guo, W. Liang, Y. Zhao, G.H. Chen, J. Phys. Chem. C **112**, 16655 (2008)
65. W.R. Duncan, C.F. Craig, O.V. Prezhdo, J. Am. Chem. Soc. **129**, 8528 (2007)
66. S. Meng, J. Ren, E. Kaxiras, Nano Lett. **8**, 3266 (2008)
67. X. Zheng, S.H. Ke, W. Yang, J. Chem. Phys. **132**, 114703 (2010)